

1 **A satellite observation-based analysis of cirrus ice**
2 **crystal number concentrations and underlying cirrus**
3 **formation mechanisms over the Tibetan Plateau**

4
5 **Kai Wang¹, Xiaocong Wang², Qianshan He³, Hong Nie⁴, Yanyu**
6 **Wang⁵, and Yonghang Chen⁶**

7 ¹College of Atmospheric Science, Nanjing University of Information Science and
8 Technology, Nanjing, China

9 ²Institute of Atmospheric Physics, Chinese Academy of Sciences, Beijing, China

10 ³Shanghai Meteorological Bureau, Shanghai, China

11 ⁴Qinghai Meteorological Service Centre, Xining, China

12 ⁵State Environmental Protection Key Laboratory of Formation and Prevention of
13 Urban Air Pollution Complex, Shanghai Academy of Environmental Sciences,
14 Shanghai, China

15 ⁶College of Environmental Science and Engineering, Donghua University, Shanghai,
16 China

17 Correspondence to: Qianshan He (oxeye75@163.com)

18
19 **Abstract.**

20 Cirrus clouds typically form in the upper troposphere and play an important role in the
21 Earth's energy balance and the atmospheric water cycle. This study utilizes
22 DARDAR-Nice data within June to August from 2006 to 2016 (except 2011),
23 combined with CloudSat cloud products and other related aerosol products, to analyze
24 the distribution characteristics and some possible formation mechanisms of ice crystal
25 number concentration (N_i) in cirrus clouds over the Tibetan Plateau (TP). The results
26 indicate that N_i over the northern TP is generally lower than that over the southern TP.
27 This contrast shows a certain connection with differences in aerosol occurrence and
28 the intensity of convective activity between the two regions. The vertical distribution
29 of N_i over the TP exhibits a V-shaped structure. When deep convective activity occurs,
30 N_i tends to increase at the same altitude compared to non-convective conditions. In

删除[凯]: characteristic

删除[凯]: , which is dominated by homogeneous freezing

1 contrast, under dust- and smoke-influenced conditions, N_i is generally lower, which
2 may be related to ice formation via heterogeneous nucleation. In addition, weak
3 vertical motion near 400 hPa over the northern TP is linked to an earlier appearance of
4 the N_i peak at altitudes below the homogeneous freezing threshold temperature ($-$
5 38° C).
6

7 **1 Introduction**

8 Cloud is the key link in the energy and water vapor balance of the
9 earth-atmosphere system and plays an important role in global weather and climate
10 change (Wang and Zhao, 1994; Stephens, 2005). Cirrus clouds are composed of a
11 large number of non-spherical ice crystal particles with a wide range coverage of
12 Earth surface (Guignard et al., 2011; Baran, 2012), which can reflect solar short-wave
13 radiation and absorb terrestrial long-wave radiation, affect the energy balance of the
14 upper troposphere and stratosphere and play an important role in the global water
15 cycle and climate change (Kienast-Sjögren et al., 2016). A definite knowledge of
16 cirrus microphysical properties and their formation mechanism is an important
17 prerequisite for deepening the understanding of global climate change.

18 The Tibetan Plateau (TP) is a highest and largest plateau of the world, known as
19 the 'roof of the world', affects significantly the climate patterns in eastern and
20 southwestern China, and even global, as well as the global water circulation system,
21 due to the unique dynamic and thermal effects. In summer, South Asian high controls
22 the TP, where the cirrus clouds show different characteristics from that in other
23 regions along the same latitude. On the one hand, the TP and its southern slope serves
24 as an important windows for troposphere-stratosphere material exchange, where the
25 frequent deep convective activities in summer have transported water vapor and
26 anthropogenic aerosol pollutants to the upper troposphere-lower stratosphere (UTLS)
27 (Fu et al., 2006; Randel et al., 2010; Chen et al., 2019). On the other hand, the
28 substantial elevation difference over the southern part of the TP and the topographic
29 uplift movement promote warm and humid airmass rising into the upper troposphere,
30 which is conducive to the occurrence and development of cirrus clouds (Zhao et al.,
31 2019; Yang et al., 2020). Also, the accumulation of aerosols is conducive to the
32 formation of cirrus ice crystals by heterogeneous nucleation.

1 So far, the study on cirrus clouds over the TP mainly focused on the
2 spatiotemporal variation characteristics, cloud height, and cirrus cloud formation
3 mechanism. Xue et al. (2018) found that the occurrence frequency, average effective
4 radius of ice particles and cloud top height reached the maximum in summer over the
5 TP using Moderate-Resolution Imaging Spectroradiometer (MODIS). Gao et al. (2003)
6 found that the occurrence frequency of cirrus clouds reached a maximum in April and
7 a minimum in November by MODIS data. Chen and Liu (2005) found that the
8 occurrence of cirrus clouds over the TP in March and April was closely related to the
9 slow uplift of warm and humid airmass to the tropopause due to topographic effect. Li
10 et al. (2005) found that deep convection activities affected by Asian Summer
11 Monsoon (ASM) were closely related to cirrus cloud formation over the TP using
12 satellite observations. Zhang et al. (2020) used Cloud-Aerosol Lidar and Infrared
13 Pathfinder Satellite Observations (CALIPSO) to investigate the generation
14 mechanism of plateau cirrus clouds, revealing that large-scale orographic uplift,
15 temperature fluctuations, and deep convection play crucial roles in their formation.

16 Previous studies have shown that the formation of cirrus ice crystals is primarily
17 governed by ~~two mechanisms: homogeneous nucleation and heterogeneous nucleation~~
18 (wang et al., 1997; Chen et al., 2000; Cantrell and Heymsfield, 2005). The
19 homogeneous freezing of supercooled water droplets or aqueous aerosol particles to
20 form ice crystals requires temperatures below approximately -38°C and sufficiently
21 high ice supersaturation (Duft and Leisner, 2004; Murray et al., 2010). While
22 heterogeneous nucleation to form ice crystals requires relatively higher ambient
23 temperature but insoluble aerosol particles (such as black carbon, dust) as
24 ice-nucleating particles (INPs) (Morris et al., 2004; Murray et al., 2010; Shi et al.,
25 2015; Fan et al., 2019).

26 Different formation mechanisms result in different effects on the microphysical
27 characteristics of cirrus ice crystals, in which ice crystal number concentration (N_i)
28 plays a crucial role in understanding and characterizing cirrus clouds (Comstock et al.,
29 2008). N_i is widely used as a key variable in cloud forecasting to predict cloud
30 evolution and is potentially closely linked to aerosol concentrations, making it an

删除[凯]: hree

删除[凯]: deep convective cloud anvil overflow (Prabhakara et al., 1993; Wang et al., 1996),

删除[凯]: Updrafts and strong horizontal currents in the upper troposphere induced by deep convective activities lead to rapidly spreading around into cloud anvils composed of ice crystal particles (Takahashi and Luo, 2012).

1 important indicator for studying the impact of aerosols on ice cloud formation (Khain
2 et al., 2000; Kay and Wood, 2008; Hendricks et al., 2011). However, current climate
3 models and satellite observations face significant limitations in obtaining and utilizing
4 N_i , which can lead to substantial biases in simulating cloud microphysical processes,
5 evaluating aerosol-cloud interactions, and calculating indirect radiative effects (Zhang
6 et al., 2013; Sourdeval et al., 2018). It is generally recognized that homogeneous
7 nucleation is the dominant mechanism ~~contributing to~~ N_i (Cantrell and Heymsfield,
8 2005). When enough INPs occurs in the atmosphere, heterogeneous nucleation
9 precedes homogeneous nucleation to form ice crystals, resulting in a consumption of a
10 large amount of water vapor and a decrease in the ambient supersaturation.
11 Suppressed homogeneous nucleation will further impede the increase in the N_i (Chen
12 et al., 2000; Kärcher and Lohmann, 2003; Shi et al., 2017). In the region of less
13 convective activities, the effective radius of ice particles increases with the increase of
14 INPs. Jin et al. (2007) used a three-dimensional storm cloud model (IAP-CSM3D) to
15 analyze the relation between convective activity and cirrus cloud, found that the
16 number concentration of ice crystal formed by deep convective cloud anvil overflow
17 decreases with a decrease in water vapor from the convective activity transports.

删除[凯]: determining

18 However, the 3D-distribution characteristics of N_i and the corresponding
19 contribution from deep convective cloud anvil overflow, homogeneous nucleation and
20 heterogeneous nucleation over the TP is not very clear. This study uses
21 liDAR-raDAR-Number concentration of ICE particles (DARDAR-Nice) data to
22 analyze the spatial distribution characteristics of medium-upper cirrus clouds in
23 summer from 2006 to 2016 (except 2011), over the TP. The formation mechanism of
24 ice particles also be explored in combination of CALIPSO satellite aerosol products
25 with reanalysis data. Furthermore, this also sheds light on the role of aerosols in the
26 upper atmosphere of the TP in the process of cirrus ice crystal formation. The results
27 will contribute to a deeper understanding of the thermodynamic effects of the TP and
28 further improve the accuracy of climate simulations.

29

30 **2 Data and methods**

2.1 Satellite observations

This study uses ten summers (June-July-August, JJA) of multi-satellite observations during 2006 to 2016, except for 2011 due to data gaps, to investigate the distribution characteristics and formation mechanism of ice crystal particles over the TP. The primary dataset is the DARDAR-Nice product, complemented by additional retrievals from CloudSat and CALIPSO observations.

The DARDAR-Nice PRO product provides high-vertical-resolution estimates of N_i retrieved along the A-Train satellite track. The retrievals are based on the VarCloud algorithm (Delanoë and Hogan, 2008; 2010), which combines observations from the Cloud Profiling Radar onboard CloudSat and the cloud-aerosol Lidar with Orthogonal Polarization (CALIOP) lidar on CALIPSO. DARDAR-Nice profiles are provided with a vertical resolution of 60 m. The product includes N_i values and corresponding uncertainty estimates for particle with size larger than 5, 25 and 100 μm . In this study, the standard error of N_i is derived directly from the `icnc_5um_error` variable, ensuring that the uncertainty associated with each profile is properly represented in the analysis. This production has been systematically and comprehensively evaluated based on theoretical considerations and a large body of in situ observations (Sourdeval et al., 2018). However, it tends to overestimate ice crystal number concentrations in cloud parcels warmer than -30°C , due to the assumption of a monomodal particle size distribution in the retrieval algorithm. To ensure the reliability of the results, this study focuses exclusively on clouds with temperatures below -30°C and discusses the N_i of ice crystals with sizes larger than 5 μm .

In addition to $N_i (>5 \mu\text{m})$, $N_i (>25 \mu\text{m})$ was also analyzed to evaluate the sensitivity of the results to the particle size threshold. Given that the DARDAR-Nice dataset predominantly samples mature or aged cirrus layers, larger ice crystals ($>25 \mu\text{m}$) may better represent the evolved stage of cloud microphysical development. Therefore, examining $N_i (>25 \mu\text{m})$ provides complementary information and helps indicate the plausible range of N_i values.

The spatial distribution and vertical structure derived from $N_i (>5 \mu\text{m})$ and $N_i (>25 \mu\text{m})$ are largely consistent, indicating that the main structural features of cirrus

1 over the Tibetan Plateau are robust across size thresholds. The primary difference lies
2 in the absolute magnitude: $N_i (>5 \mu\text{m})$ values are systematically higher by
3 approximately a factor of 2–3 compared to $N_i (>25 \mu\text{m})$, reflecting the contribution of
4 smaller ice crystals to the total population. Since $N_i (>5 \mu\text{m})$ captures a broader
5 fraction of the total ice crystal population, it is retained as the primary variable in this
6 study. The corresponding $N_i (>25 \mu\text{m})$ results are presented in the
7 supplementary material to illustrate the range of N_i values and to demonstrate that the
8 main conclusions are not sensitive to the selected particle size threshold.

设置格式[凯]: 字体: (默认) Times New Roman, (中文)
Times New Roman, 小四, 字体颜色: 自动设置

9 In addition, although ice water content (IWC) is also provided in the
10 DARDAR-Nice product, it has not been specifically validated. Therefore, this study
11 uses IWC data from the CloudSat 2B-CWC-RO product
12 (<ftp://ftp.cloudsat.cira.colostate.edu/>), for which the retrieval quality and accuracy
13 have been discussed in detail by Austin et al. (2007, 2009). Besides 2B-CWC-RO, the
14 CloudSat 2B-CLDCLASS-LIDAR product is employed, which classifies clouds into
15 eight types across ten vertical layers with a horizontal resolution of $2.5 \text{ km} \times 1.4 \text{ km}$.
16 Its classification algorithm integrates vertical and horizontal cloud structures,
17 precipitation features, cloud temperature, and MODIS radiative measurements to
18 enhance classification accuracy. These CloudSat products provide critical
19 microphysical parameters and cloud classification necessary for understanding ice
20 cloud properties.

21 CALIPSO can monitor the vertical distribution characteristics of clouds and
22 aerosols, automatically identify aerosol types, and provide global aerosol horizontal
23 distribution characteristics and vertical distribution information (Zheng et al., 2018).
24 Liu et al. (2008) also conducted aerosol detection using CALIPSO, further confirming
25 its effective aerosol detection capabilities.

26 Dust aerosols exhibit strong ice-nucleating activity and represent an important
27 global source of INPs (Hoose and Möhler, 2012; Murray et al., 2012; Ladino Moreno
28 et al., 2013). Meanwhile, sampling studies during biomass burning conducted by
29 Prenni et al. (2012) and McCluskey et al. (2014) indicate that particles from biomass
30 combustion constitute a significant regional source of INPs, particularly when other

1 effective INPs are scarce. In addition, recent observational analyses by Mamouri et al.
 2 (2023) and Ansmann et al. (2025) suggest that smoke aerosols can exert a substantial
 3 influence on ice crystal formation at altitudes while temperatures fall below -45 °C.
 4 Therefore, this study primarily focuses on the role of dust and smoke aerosols. This
 5 study employs information from the Level-2 Version 5 kmCLay standard products of
 6 the CALIPSO satellite data spanning from 2006 to 2016 (except 2011) to assess the
 7 impact of dust and smoke aerosols on the formation of cirrus clouds.

删除[凯]: 30

8 In this study, both daytime and nighttime satellite observations are included, the
 9 aerosol information is used to characterize climatological, grid-cell-averaged aerosol
 10 occurrence rather than instantaneous cloud-aerosol collocation.

11 2.2 Reanalysis Data

12 To investigate meteorological conditions, for the satellite observations, this study
 13 utilizes ERA5 reanalysis data from the European Centre for Medium-Range Weather
 14 Forecasts (ECMWF). ERA5 provides hourly global data at a spatial resolution of
 15 $0.25^\circ \times 0.25^\circ$ across 37 vertical pressure levels, covering the period from 1979 to
 16 the present (Xie et al., 2021). The key variables used in this study are specific
 17 humidity and vertical wind velocity from ERA5, as well as temperature from satellite
 18 observations. Together, these three variables are essential for analyzing
 19 meteorological conditions related to cirrus cloud formation and deep convective
 20 vertical transport.

删除[凯]: atmospheric context

删除[凯]: atmospheric

22 Table 1. Overview of the satellite datasets and data products used in this study

Source	Dataset	Variable	Period
DARDAR	DARDAR-Nice PRO	icnc_5um	2006 - 2016 (except 2011)
		icnc_5um_error	
Cloudsat	2B-CWC-RO	ice water content	
	2B-CLDCLASS-LIDAR	Cloud type(deep convection)	

设置格式[凯]: 字体: (默认) Times New Roman, (中文) Times New Roman, 加粗, 字体颜色: 自动设置

删除[凯]: **Duration**

Calipso	Level-2 Version 5 kmCLay	Aerosol type(dust 、 smoke 、 clean)
ERA5	Reanalysis	specific humidity vertical wind velocity

1

2

3 2.3 Research Methods

4 The focus area of this study is the TP and its surrounding regions, spanning from
5 66°E to 106°E and 24°N to 40°N. The original orbital data of the DARDAR-Nice
6 PRO product, 2B-CLDCLASS-LIDAR classification product and 2B-CWC-RO cloud
7 product are interpolated into grid point data with a resolution of 2° × 2° based on the
8 method outlined in Wang et al. (2023). The overall data processing workflow adopted
9 in this study is illustrated in Fig. S1 and Fig. S2. Fig. S1 outlines the procedure used
10 to derive N_i statistics, including calculations in both the horizontal and vertical
11 directions. Fig. S2 illustrates how aerosol classification data from CALIPSO are
12 combined with cirrus cloud properties retrieved from the DARDAR-Nice product.
13 These schematics provide a transparent overview of the integration and processing of
14 the various satellite datasets used in this study.

15 The 2B-CLDCLASS-LIDAR deep convective cloud product was used to
16 quantify deep convection. For each grid cell and time interval, the presence of one or
17 more deep convective clouds was counted as a single event, irrespective of the
18 number of profiles exhibiting convection. These events were then summed over all
19 intervals to yield the total number of deep convection occurrences per grid cell. For
20 the investigation of N_i , statistical analysis was conducted at intervals of 60 m, based
21 on the vertical resolution of the DARDAR-Nice PRO product. Data points with large
22 uncertainties were set to NaN to minimize bias in the statistics.

23 The horizontal distribution of N_i may be influenced by uneven sample
24 distribution resulting from the varying occurrence frequency of ice particles across
25 different layers. To address this, we normalized N_i for each grid during the ten

设置格式[凯]: 缩进: 首行缩进: 8.5 毫米

设置格式[凯]: 字体: (默认) Times New Roman, (中文)
Times New Roman, 小四, 字体颜色: 自动设置

设置格式[凯]: 字体: (默认) Times New Roman, (中文)
Times New Roman, 小四, 字体颜色: 自动设置

设置格式[凯]: 字体: (默认) Times New Roman, (中文)
Times New Roman, 小四, 字体颜色: 自动设置

设置格式[凯]: 字体: (默认) Times New Roman, (中文)
Times New Roman, 小四, 字体颜色: 自动设置

设置格式[凯]: 字体: (默认) Times New Roman, (中文)
Times New Roman, 小四, 字体颜色: 自动设置

设置格式[凯]: 字体: (默认) Times New Roman, (中文)
Times New Roman, 小四, 字体颜色: 自动设置

1 summer seasons over the TP, to obtain the horizontal distribution of N_i for cirrus
 2 clouds. The normalization process is presented in Eq. (1):

$$3 \quad y = \frac{\sum_{i=1}^{Num} x_i}{\sum_{i=1}^{Num} m_i} \quad (1)$$

4 Where x_i is the sum of N_i where the temperature is below -30°C . Num is the total
 5 number of profiles included in the analysis. m_i is the effective layers within the
 6 corresponding grid cell for which N_i is greater than 0. y is the normalized N_i in the
 7 corresponding grid.

8 To compute the vertical distribution of N_i , each profile is analyzed layer by layer.
 9 For each profile, if N_i is present in any layer, the profile is counted as 1; this count is
 10 used for normalizing the total number of profiles. For each layer, the N_i from all
 11 profiles are summed and then divided by the total number of counted profiles,
 12 yielding the normalized N_i for that layer. The detailed calculation method is given in
 13 Eq. (2):

$$14 \quad \overline{a_n} = \frac{\sum_{i=1}^{Num} a_{i,n}}{\sum_{i=1}^{Num} C_i} \quad (2)$$

15 where $\overline{a_n}$ represents the normalized N_i for layer n , $a_{i,j}$ is the N_i in layer n of
 16 profile i , C_i is the profile count ($C_i = 1$ if N_i is present in at least one layer of profile i ,
 17 and $C_i = 0$ otherwise).

18 In the absence of INPs in the atmosphere, ice crystal formation occurs primarily
 19 through homogeneous nucleation. It is generally acknowledged that temperatures near
 20 -38°C represent the threshold for homogeneous freezing of supercooled water
 21 droplets and aqueous aerosol particles under sufficiently high ice supersaturation
 22 (Duft and Leisner, 2004; Murray et al., 2010; Koop and Murray, 2016). Traditionally,
 23 the identification of homogeneous nucleation has relied primarily on temperature
 24 thresholds. However, due to the continuous dynamic growth of ice particles through
 25 condensation, accurate simulation remains challenging.

删除[凯]: .

删除[凯]: Moreover, classical nucleation theory suggests that ice formation under purely homogeneous freezing conditions is generally considered to be uncommon in the natural atmosphere (Maeda, 2021).

1 A novel approach is proposed to identify homogeneous nucleation by leveraging
2 aerosol classification data from the CALIPSO satellite over the TP during the summer
3 from 2006 to 2016. Specifically, when aerosol types are classified as ‘clean’, it
4 indicates a low concentration of INPs, favoring the dominance of homogeneous
5 nucleation in ice crystal formation. Kim et al. (2018) performed a statistical analysis
6 of different aerosol types in this product and found that ‘clean’ aerosols account for
7 only about 1% of occurrences in the CALIPSO column-level aerosol product,
8 representing background aerosol with very low concentration, which further supports
9 the validity of this assumption. Grid points identified exclusively with ‘clean’ aerosol
10 conditions are therefore interpreted as environments in which homogeneous freezing
11 may be more likely to dominate. However, clean conditions do not imply purely
12 homogeneous nucleation, and uncertainties remain regarding the relative
13 contributions of different ice formation mechanisms.

14 Although CALIPSO provides detailed vertical profiles of aerosols, this study
15 does not explicitly use the height-resolved information. Instead, the aerosol
16 occurrence is analyzed at the grid-cell level without distinguishing altitude. This
17 approach is adopted for two main reasons. First, CALIPSO’s aerosol detection is most
18 reliable in the lower troposphere, while its sensitivity decreases significantly at higher
19 altitudes due to signal attenuation and the difficulty of distinguishing aerosols from
20 thin cirrus clouds (Mao et al., 2022). Therefore, focusing on overall aerosol
21 occurrence within each grid ensures better data consistency and avoids potential
22 misclassification errors. Second, the N_i analyzed in this study corresponds to
23 temperatures below $-30\text{ }^{\circ}\text{C}$, the relevant aerosols are those that can influence cloud
24 formation through vertical transport or large-scale dynamical processes, rather than
25 being co-located at the same altitude. Hence, by integrating aerosol occurrence over
26 the entire column within the same grid, the analysis effectively captures the overall
27 influence of low-level dust or smoke aerosols on upper-tropospheric ice clouds,
28 without introducing additional uncertainty from vertical matching. Therefore, the
29 overall comparison, statistical results, and main conclusions remain robust.

删除[凯]: Grid points identified exclusively with ‘clean’
aerosol conditions are therefore considered to have undergone
only homogeneous nucleation.

3 Results and Discussion

3.1 Distribution characteristics of N_i over the TP

Based on the DARDAR-Nice PRO product, this study analyzes the spatial variation of N_i across all layers where the temperature is below -30°C during the study period. The horizontal distribution of N_i ($>5\ \mu\text{m}$) in Fig. 1 demonstrates that the average concentration over the TP is $187\ \text{L}^{-1}$ during the study period. The corresponding average concentration for N_i ($>25\ \mu\text{m}$) is $87\ \text{L}^{-1}$, which is less than half of N_i ($>5\ \mu\text{m}$) (Fig. S3). The average N_i ($>5\ \mu\text{m}$) reported here, is higher than the approximately $150\ \text{L}^{-1}$ over the TP reported by Gryspeerdt et al. (2018), who used DARDAR-Nice data from 2006 to 2013 to study global N_i ($>5\ \mu\text{m}$) but focused only on cloud-top statistics. Considering that our analysis includes all layers below -30°C , the higher N_i ($>5\ \mu\text{m}$) is reasonable and consistent with physical expectations, which also indirectly supports the reliability of our results. The average concentration in the south ($24\text{-}30^{\circ}\text{N}$, $66\text{-}106^{\circ}\text{E}$) is significantly higher than other areas, reaching $213\ \text{L}^{-1}$, with the maximum value located in the north-central region of India ($24\text{-}26^{\circ}\text{N}$, $78\text{-}80^{\circ}\text{E}$), reaching $253\ \text{L}^{-1}$. Over the north, including the Xinjiang, Inner Mongolia, the north of the Qilian Mountains and the Kunlun Mountains, N_i is only $143\ \text{L}^{-1}$, only two-thirds of N_i compared with that in the southern region. For N_i ($>25\ \mu\text{m}$), the corresponding average concentrations are $94\ \text{L}^{-1}$ in the southern region, $112\ \text{L}^{-1}$ in the north-central region of India, and $70\ \text{L}^{-1}$ in the northern areas. Compared with N_i ($>5\ \mu\text{m}$), the spatial distribution remains generally consistent, although the absolute concentrations are systematically lower.

删除[凯]:

删除[凯]: This value

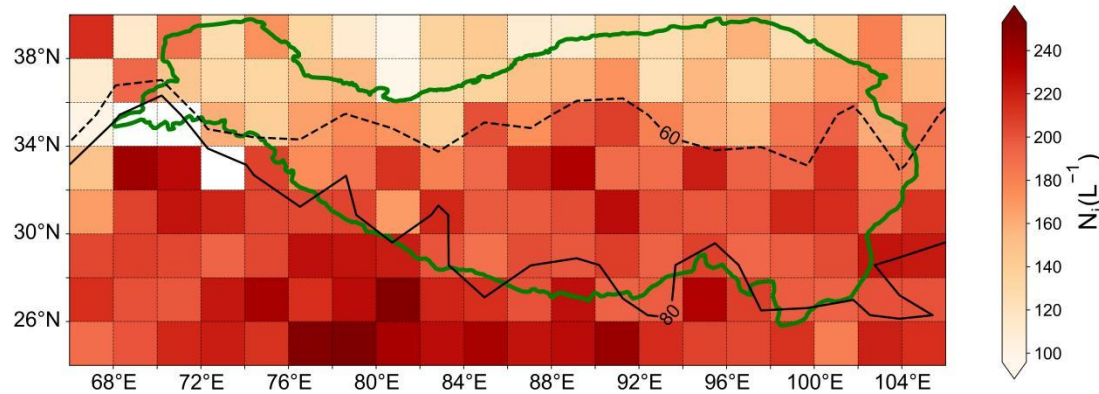


Fig. 1. Horizontal distribution of the averaged N_i during the summer from 2006 to 2016 (except

1 2011) over the TP. The green line is the border of the TP. The black solid lines represent the
2 standard error of 80 L^{-1} and the black dotted line represents the value of 60 L^{-1} .

3

4 We investigated the relationship between the incidence of deep convective clouds,
5 INPs, and N_i at all grid points over the TP based on the different formation
6 mechanisms of cirrus clouds. As shown in Fig. 2a, deep convection occurrences
7 (DCO) is significantly higher in the southern and southeastern regions of the Plateau,
8 where the N_i tend to be elevated (Fig. 1). Also, N_i revealed a positive nonlinear
9 relationship with DCO, with a coefficient of determination (R^2) of 0.55 ($p < 0.01$) and a
10 root mean square error (RMSE) of 24.03 L^{-1} , indicating that deep convective activity
11 plays a significant role in modulating N_i over the TP. During the ASM, frequent deep
12 convection in the southern TP facilitates the transport of warm, moist air and water
13 droplets from the Indian Ocean and the Bay of Bengal to higher altitudes (He et al.,
14 2019). Under moist conditions, ascending air parcels are more likely to experience a
15 prolonged period of ice supersaturation, thereby increasing the probability of
16 exceeding the supersaturation threshold required for homogeneous ice nucleation. In
17 humid environments, air parcels can therefore maintain supersaturated conditions for
18 a longer duration, making homogeneous nucleation more likely to dominate under
19 such circumstances (Zhao et al., 2018). By contrast, heterogeneous nucleation is
20 initiated by INPs and typically requires a lower ice supersaturation threshold,
21 allowing it to occur earlier during ascent (DeMott et al., 2010). As a result, in
22 environments with abundant water vapor, homogeneous nucleation may gain a
23 relative advantage in competition with heterogeneous nucleation, favouring the
24 formation of higher N_i .

25 This interpretation is consistent with the relatively high N_i observed over the
26 southern TP during summer. However, within an observational framework alone, the
27 respective contributions of dynamical conditions, aerosol properties, and
28 thermodynamic processes cannot be fully disentangled. The interpretation presented
29 here should therefore be regarded as a qualitative explanation based on physical
30 consistency rather than a definitive attribution.

1 In addition to convective activity, the presence of INPs also plays a critical role in
2 modulating N_i over the TP. Zhao et al. (2018), using nine years of satellite
3 observations, demonstrated that ice crystal formation is regulated not only by the
4 availability of INPs but also by ambient water vapor conditions. This highlights the
5 important role of moisture as a prerequisite for cirrus cloud evolution, while
6 emphasizing that high water vapour availability alone is not sufficient to guarantee ice
7 formation. Ice nucleation can only occur when the ice saturation ratio exceeds the
8 threshold required for freezing; without reaching this threshold, no ice formation is
9 possible (Gettelman et al., 2010). As a result, moisture should be regarded as a
10 necessary background condition rather than a direct or sufficient driver of ice crystal
11 formation.

12 Consequently, when investigating the relationship between INPs and N_i , directly
13 comparing INPs and N_i across all grid cells may lead to misleading interpretations.
14 This is because differing atmospheric conditions, particularly variations in moisture
15 and the development of ice supersaturation, can strongly influence whether ice
16 formation occurs. For example, high N_i in one grid cell may primarily reflect
17 favourable moisture conditions that allow supersaturation to be achieved, rather than
18 an enhanced influence of INPs, whereas in another grid cell the potential effect of
19 INPs may be masked if the supersaturation threshold is not exceeded.

20 In principle, restricting the analysis to grid cells with broadly similar atmospheric
21 conditions would allow a more direct comparison. However, the TP exhibits
22 pronounced spatial heterogeneity, especially between its northern and southern
23 regions. To partially account for differences in moisture-related thermodynamic
24 conditions, this study introduces the IWC confined INPs concentration (ICIC),
25 defined as the logarithm of the ratio between the occurrence number of smoke (or dust)
26 particles and IWC within each grid cell (Eq. 3). This formulation aims to reduce the
27 confounding influence of IWC on the apparent N_i -INPs relationship. To further
28 demonstrate the robustness of this normalization, we compute the partial correlation
29 between INPs and N_i after removing the effect of IWC. Specifically, the partial
30 correlation coefficient is calculated by statistically removing the linear effect of IWC

设置格式[凯]: 字体: 倾斜

设置格式[凯]: 字体: 倾斜, 下标

删除[凯]: By standardization, this metric improves the comparability of the analysis to some extent.

设置格式[凯]: 字体: (默认) Times New Roman, (中文) 宋体, 小四, 字体颜色: 自动设置

1 from both N_i and ICIC across all grid cells and then computing the correlation
2 between the residuals. This approach does not eliminate the physical influence of
3 IWC on N_i , but allows an evaluation of the N_i -INPs relationship independent of the
4 first-order linear contribution of IWC. The resulting partial correlation coefficient ($r =$
5 -0.38) indicates that a relationship between ICIC and N_i remains after accounting for
6 IWC, although IWC itself continues to exert a strong influence.

设置格式[凯]: 字体: (默认) Times New Roman, (中文)
宋体, 小四, 字体颜色: 自动设置

设置格式[凯]: 字体: (默认) Times New Roman, (中文)
宋体, 小四, 字体颜色: 自动设置

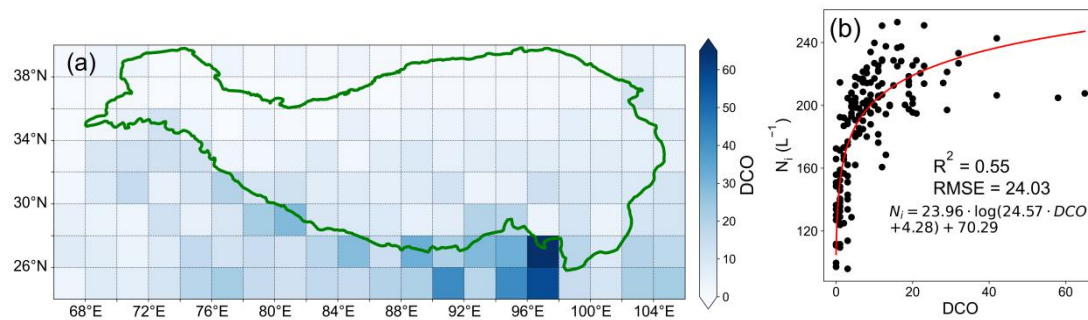
删除[凯]: The resulting coefficient, $r = -0.38$, confirms that
the ICIC formulation effectively reduces moisture-related
confounding.

$$7 \quad ICIC (type) = \log \left(\frac{type_{event}}{IWC} \right) \quad (3)$$

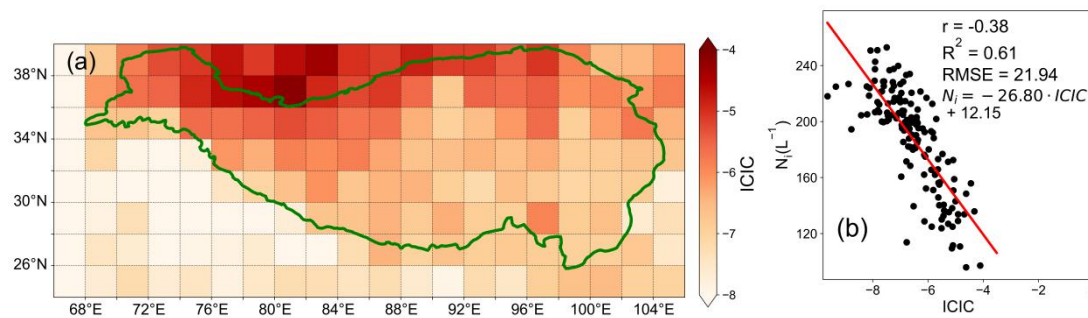
8 Where $type$ is dust or smoke, $type_{event}$ is the number of events of that aerosol type,
9 and $ICIC(type)$ is the ICIC value corresponding to that aerosol type in the
10 corresponding grid.

11 Fig.3a shows the spatial distribution of this metric, revealing that ICIC is
12 predominantly concentrated in the northern part of the Plateau, with significantly
13 lower values in the south. Moreover, an inverse nonlinear relationship is observed
14 between ICIC and N_i , with a coefficient of determination (R^2) of 0.61 ($p < 0.01$) and a
15 root mean square error (RMSE) of 22 L^{-1} , indicates that the quantity of ICIC has a
16 significant impact on the N_i over the TP. While the N_i mainly arises from
17 homogenization nucleation, heterogeneous nucleation of INPs promotes the formation
18 of ice crystals (Khvorostyanov et al., 2006; DeMott et al., 2010) by absorbing a large
19 amount of water vapor and destroying the conditions for homogeneous nucleation.
20 The inhibitory effect of heterogeneous nucleation on homogeneous nucleation
21 becomes more pronounced with an increase in INPs content, leading to a lower N_i .
22 These two factors, namely the increased convective cloud frequency in the south and
23 the elevated INPs levels in the north, are the primary contributors to the observed
24 spatial pattern of N_i , which tends to be higher in the south and lower in the north.

25



1
2 **Fig. 2. (a)** Horizontal distribution of DCO and **(b)** the relationship with N_i during the summer
3 from 2006 to 2016 (except 2011) over the TP.



4
5 **Fig. 3. (a)** Horizontal distribution of the ICIC and **(b)** the relationship with N_i during the summer
6 from 2006 to 2016 (except 2011) over the TP. $r(-0.38)$ in this figure is the partial correlation
7 coefficient between INPs and N_i after removing the effect of IWC.

8

9 **3.2 Generation mechanism of ice crystal formation**

10 **3.2.1 Contribution of the homogeneous nucleation**

11 Due to the condensation growth of cirrus cloud ice crystals in the upper
12 atmosphere after nucleation, the observed ice crystal particle size in the satellite
13 observation dataset only represents the post-growth effect, rendering it impossible to
14 distinguish the contribution of different nucleation mechanisms to ice crystal size.
15 Thus, this study considered the contribution of different nucleation mechanisms to the
16 formation of cirrus cloud ice crystals by examining changes in the N_i .

17 N_i for each vertical layer is calculated using Eq. (2), and Fig. 4 depicts the vertical
18 distribution of the N_i for all satellite-retrieved cases ('all') and for clean aerosol
19 conditions ('clean'). Here, 'all' refers to N_i retrieved from all available satellite
20 observations regardless of aerosol type, whereas 'clean' refers to cases where
21 CALIOP does not indicate the presence of dust or smoke and the aerosol type is

删除[凯]: from

删除[凯]: satellite observations

删除[凯]: homogeneous nucleation

设置格式[凯]: 字体: 倾斜

设置格式[凯]: 字体: 倾斜, 下标

删除[凯]: In

1 classified as 'clean'. Under clean conditions, ice formation is interpreted as being
2 more likely influenced by homogeneous freezing. However, in this situation, purely
3 homogeneous nucleation cannot be assumed, and uncertainties remain regarding the
4 relative contributions of different ice formation pathways.

删除[凯]: , ice formation is assumed to occur via homogeneous freezing

5 The satellite observations indicate that the N_i initially slowly increases with
6 height and reaches its maximum of 68 L^{-1} at 14 km, and follows a decreasing trend
7 with height up to 19 km. The vertical variation of N_i under clean conditions and for all
8 satellite-retrieved cases, both show an overall 'V' shaped distribution. However, N_i
9 under clean conditions is generally higher than that for all satellite-retrieved cases, at
10 corresponding altitudes. Specifically, the N_i under clean conditions, peaks at 14 km
11 with a value of 94 L^{-1} , which coincides with the altitude of the observed peak.

删除[凯]: from homogeneous nucleation and observation

删除[凯]:

删除[凯]: derived from homogeneous nucleation is consistently higher than the satellite observations

12 It is widely accepted that the formation of larger ice crystals through
13 heterogeneous nucleation processes takes precedence over homogeneous nucleation
14 (Shi et al., 2017; Barahona and Nenes, 2009). In fact, heterogeneous nucleation is the
15 dominant ice formation mechanism at temperatures above $-38 \text{ }^\circ\text{C}$, whereas
16 homogeneous nucleation occurs only when the temperature drops below $-38 \text{ }^\circ\text{C}$ and
17 when there are no INPs. Although homogeneous freezing may represent an important
18 contributor under sufficiently cold and supersaturated conditions, (Cantrell and

删除[凯]: the number concentration from homogeneous nucleation

19 Heymsfield, 2005), heterogeneous nucleation has lower activation requirements and
20 may occur earlier, potentially consuming water vapor and influencing subsequent ice

删除[凯]: homogeneous nucleation is the major contributor to the N_i

21 formation. Under this interpretation, the N_i for all satellite-retrieved cases being lower
22 than that expected under conditions more likely influenced by homogeneous freezing

删除[凯]: observed

删除[凯]: favorable for

23 could be consistent with the influence of heterogeneous nucleation. However,
24 alternative explanations cannot be excluded. For example, lower N_i may also reflect
25 weaker or less frequent updrafts, which would limit the development of high ice
26 supersaturation, or differences in cloud origin, such as a predominance of in-situ
27 cirrus with limited contribution from liquid-origin ice detrained from deep convective
28 updrafts (Gryspeerdt et al., 2018; Lyu et al., 2025).

29 Additionally, it is also worth noting that the N_i for all satellite-retrieved cases
30 slightly exceeds the values from N_i under clean conditions, below approximately 12

删除[凯]: observed

删除[凯]: homogeneous nucleation

1 km. This is likely because homogeneous nucleation has not yet become dominant in
 2 this layer, while the observed N_i reflects prior heterogeneous nucleation events that
 3 produced a relatively large number of ice crystals. Once homogeneous nucleation
 4 becomes active with decreasing temperature, it rapidly generates N_i values
 5 substantially higher than all satellite-retrieved cases. From a trend perspective, the 'V'
 6 shape vertical distribution and the peak position of N_i is likely determined by the role
 7 of homogeneous nucleation, while the specific values at different altitudes likely
 8 reflects the combined and interacting effects of homogeneous nucleation and
 9 heterogeneous nucleation.

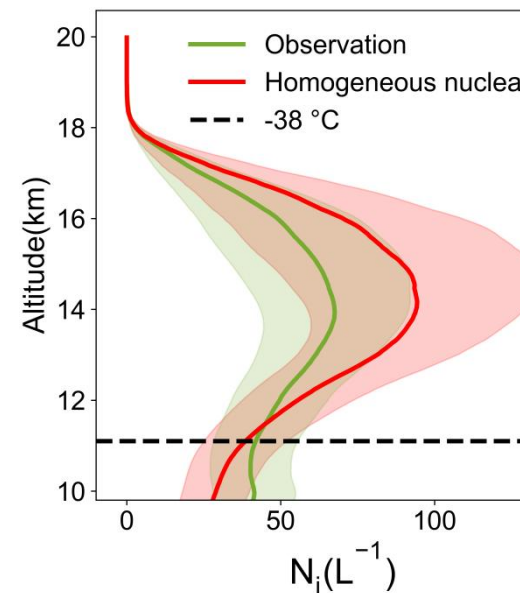
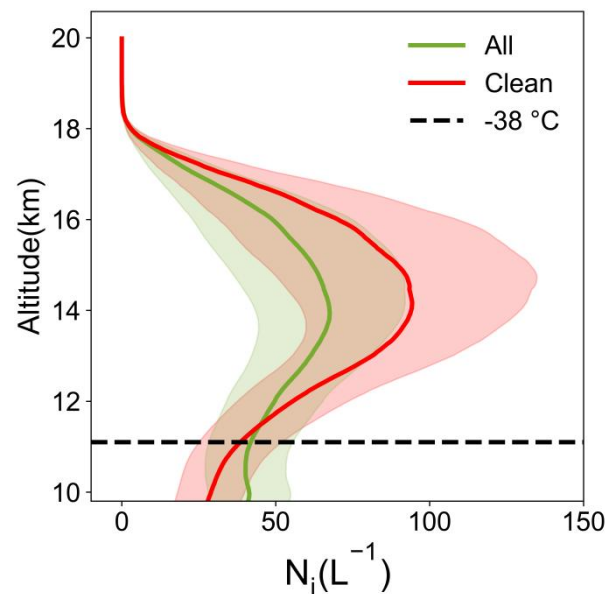
设置格式[凯]: 非上标/ 下标

删除[凯]: a

删除[凯]: N_i

删除[凯]: observed

删除[凯]: are determined by the combined effect of



11 **Fig. 4.** Vertical profiles of N_i for all satellite-retrieved cases ('all') and for clean aerosol conditions
 12 ('clean'), with light shading indicating the standard error range.

删除[凯]:

设置格式[凯]: 字体: (默认) Times New Roman, (中文) Times New Roman, 倾斜, 字体颜色: 自动设置

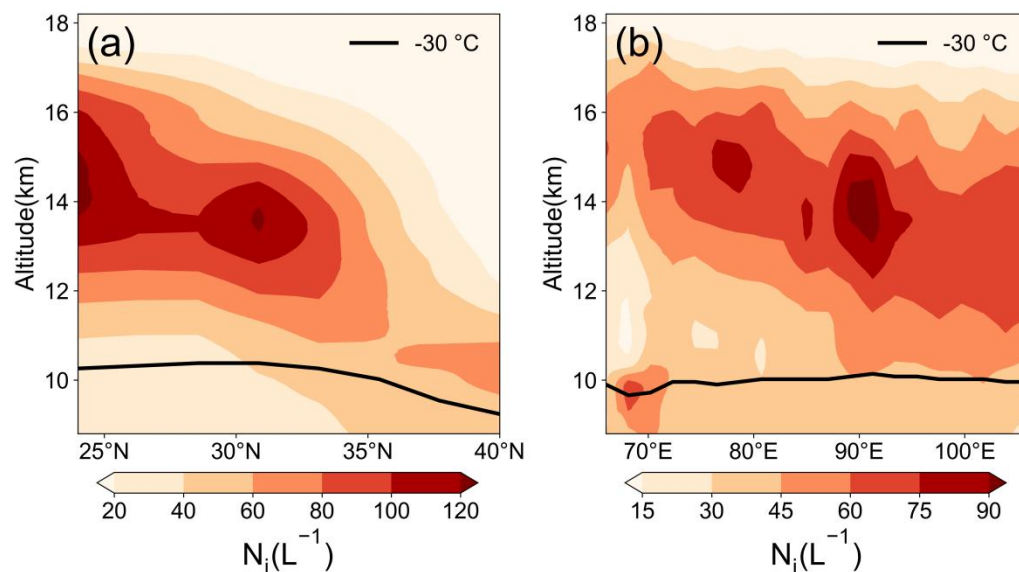
设置格式[凯]: 字体: (默认) Times New Roman, (中文) Times New Roman, 倾斜, 字体颜色: 自动设置, 下标

删除[凯]: observed and homogeneously nucleated N_i

14 To further investigate the vertical distribution characteristics of N_i , this study
 15 analyzes its spatial distribution across different latitudes and longitudes based on Fig.
 16 5. In the zonal cross-section (Fig. 5a), the N_i exhibits a pronounced maximum near 14
 17 km altitude between 28°N and 33°N, exceeding 120 L^{-1} . Additionally, in the
 18 meridional cross-section (Fig. 5b), a peak N_i of over 90 L^{-1} is observed near 90°E, also
 19 centered at 14 km altitude.

20 Together, these zonal and meridional distributions reveal a consistent vertical
 21

1 structure, with peak N_i occurring near 14 km, which could be influenced by
 2 homogeneous nucleation processes that dominate at these altitudes (Fig. 4). In
 3 contrast, N_i exhibits significant variability across both latitudinal and longitudinal
 4 directions, which may be related to the spatial distribution of water vapor and certain
 5 meteorological factors, such as vertical wind velocity, providing a foundation for the
 6 subsequent analysis in this study.



7
 8 **Fig. 5.** (a) The zonal distribution of N_i from 86 to 102°E for each latitude and (b) the meridional
 9 distribution of N_i from 24 to 40°N for each longitude.

10

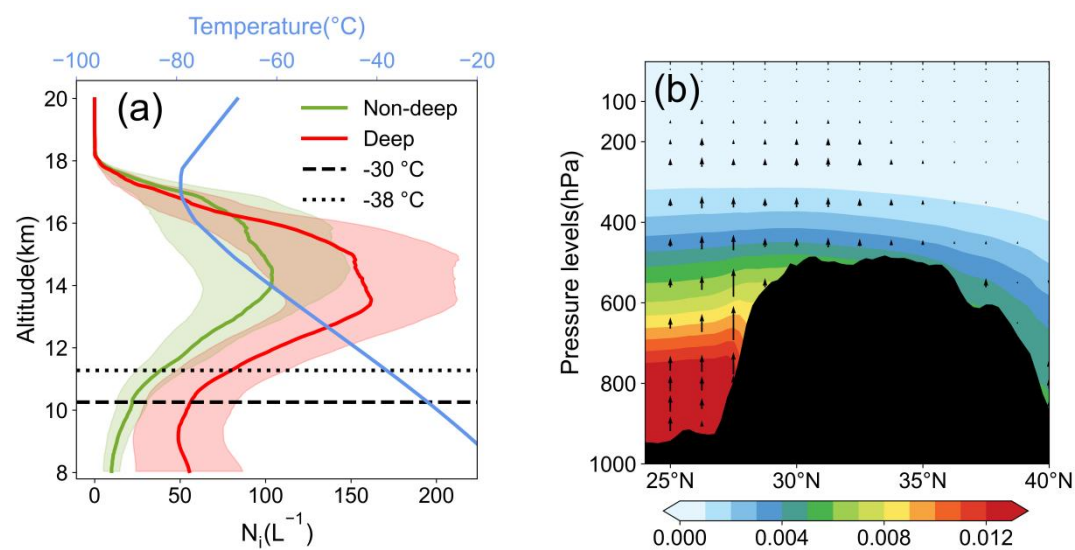
11 3.2.2 The effect of deep convective activity

12 In addition to homogeneous nucleation, deep convective cloud anvils are another
 13 significant source of ice crystal formation in the atmosphere. Fig. 6a compares the
 14 altitude-averaged N_i under different deep convective cloud conditions, based on all
 15 grid points across the TP where the incidence of deep convection exceeds 5% (Fig.
 16 2a). These selected regions represent areas with relatively frequent convective
 17 activity.

18 During summer, the tropopause height over the Tibetan Plateau typically ranges
 19 from about 16 - 18 km (Sun et al., 2021), providing an important vertical reference for
 20 cirrus cloud development. The top of cirrus clouds can develop near 18 km with a
 21 relatively low N_i for the case of non-deep convection activity, and at 14 km, reaches

1 its peak of 104 L^{-1} . When deep convection activity occurs, the N_i at the same altitude
 2 is significantly higher, and at 14 km, reaches its peak of 162 L^{-1} . During summer,
 3 strong upward motions over the southern TP can transport both moist air and
 4 pre-existing ice crystals from the lower troposphere (below 12 km) into the upper
 5 troposphere via convective outflow anvils. These processes may create favorable
 6 conditions for enhanced N_i , while homogeneous nucleation may additionally occur
 7 under sufficiently cold and supersaturated conditions. It is therefore suggested that the
 8 observed N_i peak near 14 km is associated with the combined effects of convective
 9 transport, dynamical accumulation, and ice formation processes. At 14 km (about 140
 10 hPa), where the vertical wind speed is nearly zero, N_i accumulates significantly above
 11 this level, while a substantial amount is transported upward from below 14 km. This
 12 upward transport, combined with the accumulation, results in the peak at 14 km (Fig.
 13 4b). Satellite observations also indicate that during the development of deep
 14 convective clouds, approximately 95% of the cloud tops are located at or below 16 km.
 15 This vertical distribution suggests that the influence of deep convection is mainly
 16 confined below 16 km. Consequently, N_i above this level remains relatively
 17 unchanged, indicating limited impact from convective processes at higher altitudes.

18



19

20 **Fig. 6.** (a) Vertical profile of the N_i affected by DCO and (b) the zonal distribution of vertical
 21 winds averaged from 86 to 102°E for each latitude. The contour is specific humidity (kg kg^{-1}).

1

2 3.2.3 Heterogeneous nucleation effect of INPs

3 In the northern part of the TP, convective activity is relatively weak, but dust
4 aerosol content is high (Fig. 7a). The increase in N_i is primarily attributed to
5 heterogeneous nucleation induced by INPs. Considering the frequent dust activity in
6 this region, we selected grid points with ICIC(dust) greater than -5 as the primary
7 study area. These grid points are predominantly located in the northern Plateau,
8 adjacent to Xinjiang, a typical semi-arid region characterized by abundant dust
9 aerosols. These dust particles facilitate water vapor adsorption in the lower
10 atmosphere and promote ice crystal formation through heterogeneous nucleation
11 (Huang et al., 2021; Hoose and Möhler, 2012).

12 It should be emphasized that the aerosol information used in this study represents
13 column-level aerosol classification within each grid cell, rather than vertically
14 co-located aerosol–cloud interactions. Dust aerosols are predominantly distributed in
15 the lower troposphere. Therefore, the comparison between upper-tropospheric N_i and
16 aerosol occurrence reflects statistical associations at the grid-cell scale, which may be
17 influenced by vertical transport and large-scale dynamical processes, rather than direct,
18 instantaneous interactions at the same altitude.

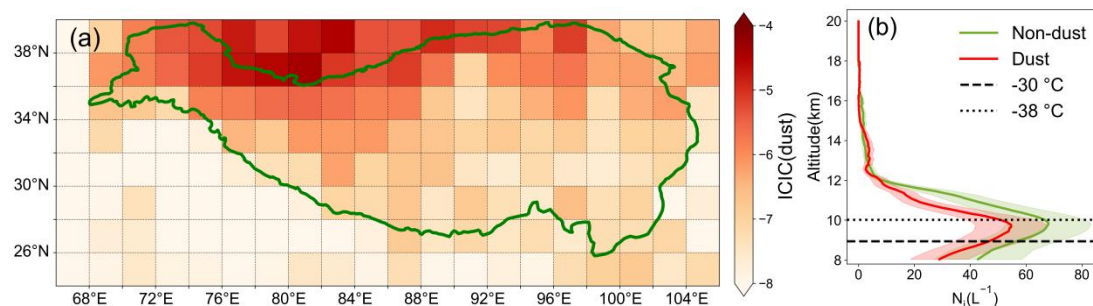
19 Fig. 7b illustrates the effect of dust aerosol particles on N_i in this area. The results
20 suggest that the presence of dust is associated with a reduction of N_i in cirrus clouds,
21 with concentrations above 12 km becoming very small. During non-dust periods,
22 although INPs remain present, their activation efficiency may be relatively high,
23 allowing a large fraction of aerosol ice nuclei to be activated, resulting in weaker
24 suppression of ice crystal formation. In contrast, elevated dust concentrations in the
25 lower atmosphere may enhance heterogeneous nucleation, thereby consuming
26 available water vapor and potentially inhibiting additional ice crystal formation,
27 which could lead to a reduction of N_i . Within this interpretative framework, N_i during
28 non-dust periods tends to be higher than during dust conditions. However, due to
29 limited water vapor in this region, a large fraction of moisture may already be
30 depleted in the lower atmosphere, which could contribute to very low N_i above 12 km.

设置格式[凯]: 字体: (默认) Times New Roman, (中文)
Times New Roman, 小四, 字体颜色: 自动设置

设置格式[凯]: 字体: (默认) Times New Roman, (中文)
Times New Roman, 小四, 字体颜色: 自动设置

设置格式[凯]: 字体: (默认) Times New Roman, (中文)
Times New Roman, 字体颜色: 自动设置

1 Consequently, the suppressive effect of heterogeneous nucleation may limit ice crystal
 2 formation through homogeneous nucleation at higher altitudes, making cirrus cloud
 3 development more difficult in these upper layers. In regions with low water vapor
 4 content, INPs may play an important role in modulating N_i .



5
 6 **Fig. 7. (a)** Horizontal distribution of ICIC(dust) and **(b)** the vertical profile of the N_i affected by
 7 dust and non-dust events. Here, ‘non-dust’ refers to all cases in which CALIPSO does not detect
 8 dust aerosols, including clean aerosol conditions.

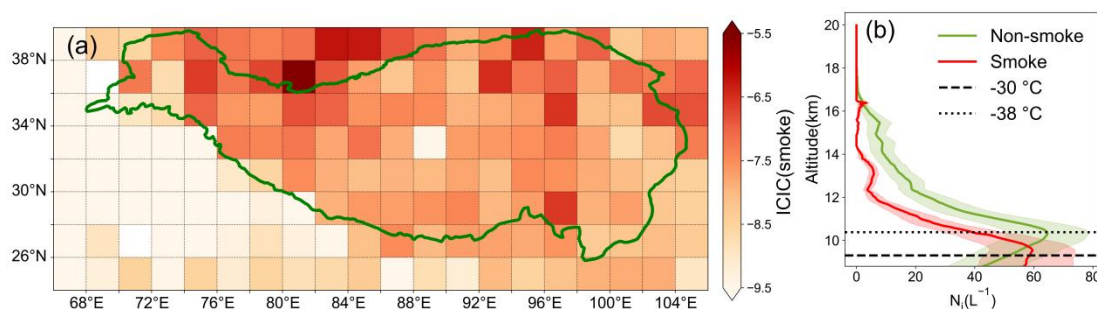
9

10 Besides dust aerosol, smoke aerosol particles generated by human activities are
 11 considered another potential source of heterogeneous nucleation for cirrus clouds over
 12 the TP. In this research, grid points with ICIC(smoke) greater than -6.5 were selected
 13 as the primary research region to examine the possible influence of smoke INPs on N_i
 14 (Fig. 8a).

15 It is observed that the presence of smoke aerosols is associated with a decrease in
 16 N_i , with the maximum vertical extent of cirrus clouds limited to around 14 km (Fig.
 17 8b). One possible interpretation is that, during smoke events, ice crystal formation in
 18 the lower atmosphere may be influenced by smoke-derived INPs, under which
 19 heterogeneous nucleation could become more active. The relatively high abundance
 20 of smoke INPs may enhance competition among ice particles, potentially suppressing
 21 additional ice crystal formation and resulting in lower N_i compared to non-smoke
 22 conditions. In this hypothetical framework, smoke INPs may be efficiently activated
 23 through heterogeneous nucleation, while any remaining water vapor could still
 24 contribute to ice formation via homogeneous nucleation. From this perspective, N_i
 25 tends to be higher during non-smoke periods, when fewer INPs may lead to weaker

1 suppression effects. However, due to the inherently low water vapor content in this
2 region, the vertical development of cirrus clouds appears to be constrained, and even
3 during non-smoke periods, the maximum cloud height remains limited to
4 approximately 17 km.

5 Homogeneous nucleation is often associated with a peak in N_i near 14 km.
6 However, under dust and smoke conditions, such a peak is not clearly observed. One
7 possible explanation is that dust and smoke aerosols are mainly concentrated over the
8 northern TP, where the vertical wind speed around 400 hPa is relatively weak (Fig.
9 6b). Reduced vertical transport may limit the upward redistribution of ice crystals,
10 thereby influencing the vertical structure of N_i .



11
12 **Fig. 8.** (a) Horizontal distribution of ICIC(smoke) and (b) the vertical profile of the N_i affected by
13 smoke and non-smoke events. Here, ‘non-smoke’ refers to all cases in which CALIPSO does
14 not detect aerosols, including clean aerosol conditions.

15

16 4 Conclusion

17 This study analyzed the distribution characteristics and formation mechanism of
18 cirrus cloud ice crystals during the summer of 2006 to 2016 (except 2011) over the TP,
19 mainly using DARDAR-Nice data combined with aerosol product data.

20 The main conclusions are summarized as follows: (1) N_i shows pronounced
21 spatial variability across the TP, with generally higher values over the southern TP
22 than over the northern TP. This contrast is statistically associated with differences in
23 large-scale meteorological conditions, including more frequent deep convection over
24 the southern TP, whereas the northern TP is characterized by more frequent aerosol
25 occurrence and lower N_i .

1 (2) The vertical distribution of N_i exhibits a characteristic V-shaped structure,
2 consistent with statistical signatures expected under conditions favorable for
3 homogeneous freezing. The values of N_i at varying altitudes are likely determined by
4 the combined effects of both homogeneous and heterogeneous nucleation.

5 (3) Regions influenced by deep convection tend to exhibit higher N_i at a given
6 altitude than non-convective regions. This behavior is consistent with the role of
7 convective outflow anvils in transporting moisture and pre-existing ice crystals into
8 the upper troposphere, while homogeneous freezing may additionally occur under
9 sufficiently cold and supersaturated conditions.

10 (4) Under dust and smoke influenced conditions, ice formation in the lower
11 atmosphere is statistically associated with heterogeneous nucleation occurring prior to
12 homogeneous freezing, and N_i is generally lower than non-dust(smoke) conditions.
13 This behavior may be related to early vapor consumption, differences in vertical
14 motion, and sedimentation effects. These interpretations represent one possible
15 explanation of the observed.

16 Several limitations should be noted. This study integrates several validated
17 satellite retrieval products in the analysis. Nevertheless, differences in retrieval
18 methodologies and sensor sensitivities among these products introduce inherent
19 uncertainties, which may affect the quantitative interpretation of the results to some
20 extent. In addition, the use of multi-year climatological averages smooths event-scale
21 extremes associated with strong updrafts or short-lived dynamical processes. Aerosol
22 information represents grid-cell-scale and climatological conditions rather than
23 instantaneous cloud-aerosol interactions. Consequently, the results should be regarded
24 as hypothesis-driven and exploratory, providing statistical context and motivation for
25 future studies combining satellite observations, in-situ measurements, and modeling.

26 **Code and data availability**

27 Code and data can be provided by the corresponding author on request.

28 **Author contributions**

设置格式[凯]: 缩进: 首行缩进: 0 字符

设置格式[凯]: 字体: (默认) Arial, (中文) Times New Roman, 小四, 加粗, 图案: 清除(自动设置), 字体颜色: 自动设置, 字距调整: 1 磅

设置格式[凯]: 段落间距段前: 0 磅, 段后: 0 磅, 行距: 1.5 倍行距, 图案: 清除(自动设置), 无孤行控制

设置格式[凯]: 字体: (默认) Arial, (中文) Times New Roman, 小四, 加粗, 字体颜色: 自动设置

设置格式[凯]: 字体: (默认) Times New Roman, (中文) 宋体, 10 磅, 图案: 清除(自动设置), 字体颜色: 自动设置, (复杂文种) 阿拉伯语(沙特阿拉伯)

设置格式[凯]: 字体: (默认) Times New Roman, 10 磅, 字体颜色: 自动设置, (复杂文种) 阿拉伯语(沙特阿拉伯)

设置格式[凯]: 缩进: 首行缩进: 0 字符

设置格式[凯]: 字体: (默认) Arial, (中文) Times New Roman, 小四, 加粗, 字体颜色: 自动设置

设置格式[凯]: 字体: (默认) Arial, 加粗, 字体颜色: 自动设置

1 All the authors made contributions to this research work and manuscript. KW, XW, and QH conceived
2 and designed the research. KW performed the data analysis and drafted the manuscript. HN and YW
3 contributed to data processing and interpretation. QH and YC supervised the study. All authors
4 participated in scientific discussions, revised the manuscript, and approved the final version for
5 publication.

设置格式[凯]: 字体: (默认)Times New Roman, 10 磅, 字距调整: 0 磅

设置格式[凯]: 缩进: 首行缩进: 0 字符, 行距: 单倍行距, 孤行控制

6

7 **Competing interests**

设置格式[凯]: 字体: (中文)宋体, 10 磅, 字距调整: 0 磅

设置格式[凯]: 缩进: 首行缩进: 0 字符

8 The contact author has declared that none of the authors has any competing interests.

设置格式[凯]: 字体: (中文)宋体, 字距调整: 0 磅

10 **Acknowledgements**

设置格式[凯]: 缩进: 首行缩进: 0 毫米, 行距: 单倍行距, 孤行控制

11 This study was supported by the National Natural Science Foundation of China (NSFC, Grant Numbers:
12 42330603), the Open Research of Key Laboratory of Intelligent Meteorological Observation
13 Technology in China Meteorological Administration (ZNGC2024ZD02), the Science and Technology
14 Planning Program of Xinjiang (2022E01047), National Natural Science Foundation of China
15 (42030612 and 42175179), and the Natural Science Foundation of Shanghai (22ZR1404000). The
16 authors gratefully acknowledge the ECMWF for providing ERA5 data, and the NASA for providing
17 CloudSat and CALIPSO data. In addition, the DARDAR-Nice product used in this study was obtained
18 from the AERIS/ICARE data center.

设置格式[凯]: 缩进: 首行缩进: 0 字符

设置格式[凯]: 字体: (默认)Arial, (中文)Times New Roman, 小四, 加粗, 非倾斜, 字体颜色: 自动设置, 字距调整: 1 磅

设置格式[凯]: 左, 行距: 1.5 倍行距, 无孤行控制

删除[凯]: .

20 **References**

21 Ansmann, A., Jimenez, C., Knopf, D. A., Roschke, J., Bühl, J., Ohneiser, K., and Engelmann, R.: Impact of
22 wildfire smoke on Arctic cirrus formation–Part 2: Simulation of MOSAiC 2019–2020 cases, Atmos. Chem.
23 Phys., 25, 4867-4884, 2025.

24 Austin, R. T., Heymsfield, A. J., and Stephens, G. L.: Retrieval of ice cloud microphysical parameters using the
25 CloudSat millimeter-wave radar and temperature, J. Geophys. Res., 114, doi:10.1029/2008JD010049, 2009.

26 Austin, R. T.: Level 2B radar-only cloud water content (2B-CWC-RO) process description document, Data
27 Processing Center, 24, 2007.

28 Barahona, D. and Nenes, A.: Parameterizing the competition between homogeneous and heterogeneous freezing in
29 ice cloud formation-polydisperse ice nuclei, Atmos. Chem. Phys., 9, 5933-5948, 2009.

30 Baran, A. J.: From the single-scattering properties of ice crystals to climate prediction: A way forward, Atmos. Res.,
31 112, 45-69, 2012.

32 Cairo, F., Krämer, M., Afchine, A., Di Donfrancesco, G., Di Liberto, L., Khaykin, S., Lucaferri, L., Mitev, V., Port,
33 M., Rolf, C., Snels, M., Spelten, N., Weigel, R., and Borrmann, S.: A comparative analysis of in situ
34 measurements of high-altitude cirrus in the tropics, Atmos. Meas. Tech., 16, 4899-4925, 2023.

35 Cantrell, W. and Heymsfield, A.: Production of ice in tropospheric clouds: A review, Bull. Am. Meteorol. Soc., 86,

1 795-808, 2005.

2 Chen, B. and Liu, X.: Seasonal migration of cirrus clouds over the Asian Monsoon regions and the Tibetan Plateau
3 measured from MODIS/Terra, *Geophys. Res. Lett.*, 32, doi:1029/2004GL020868, 2005.

4 Chen, Q. L., Gao, G. L., Li, Y., Cai, H. K., Zhou, X., and Wang, Z. L.: Main detrainment height of deep convection
5 systems over the Tibetan Plateau and its southern slope, *Adv. Atmos. Sci.*, 36, 1078-1088, 2019.

6 Chen, Y., DeMott, P. J., Kreidenweis, S. M., Rogers, D. C., and Sherman, D. E.: Ice formation by sulfate and
7 sulfuric acid aerosol particles under upper-tropospheric conditions, *J. Atmos. Sci.*, 57, 3752-3766, 2000.

8 Comstock, J. M., Lin, R. F., Starr, D. O. C., and Yang, P.: Understanding ice supersaturation, particle growth, and
9 number concentration in cirrus clouds, *J. Geophys. Res. Atmos.*, 113, D23211, 2008.

10 Delanoë, J., and Hogan, R. J.: A variational scheme for retrieving ice cloud properties from combined radar, lidar,
11 and infrared radiometer, *J. Geophys. Res.*, 113, D07204, 2008.

12 Delanoë, J., and Hogan, R. J.: Combined CloudSat-CALIPSO-MODIS retrievals of the properties of ice clouds, *J.*
13 *Geophys. Res.*, 115, D00H29, 2010.

14 DeMott, P. J., Prenni, A. J., Liu, X., Kreidenweis, S. M., Petters, M. D., Twohy, C. H., Richardson, M., Eidhammer,
15 T., and Rogers, D.: Predicting global atmospheric ice nuclei distributions and their impacts on climate, *Proc.*
16 *Natl. Acad. Sci.*, 107, 11217-11222, 2010.

17 Duft, D., and Leisner, T.: Laboratory evidence for volume-dominated nucleation of ice in supercooled water
18 microdroplets, *Atmos. Chem. Phys.*, 4, 1997-2000, 2004.

19 Fan, F., Zhang, S., Peng, Z., Chen, J., Su, M., Moghtaderi, B., and Doroodchi, E.: Numerical investigation of
20 heterogeneous nucleation of water vapour on PM10 for particulate abatement, *Can. J. Chem. Eng.*, 97,
21 930-939, 2019.

22 Fu, R., Hu, Y., Wright, J. S., Jiang, J. H., Dickinson, R. E., Chen, M., Filipiak, M., Read, W. G., Waters, J. W., and
23 Wu, D. L.: Short circuit of water vapor and polluted air to the global stratosphere by convective transport over
24 the Tibetan Plateau, *Proc. Natl. Acad. Sci.*, 103, 5664-5669, 2006.

25 Gao, B. C., Yang, P., Guo, G., Park, S. K., Wiscombe, W. J., and Chen, B.: Measurements of water vapor and high
26 clouds over the Tibetan Plateau with the Terra MODIS instrument, *IEEE Trans. Geosci. Remote Sens.*, 41,
27 895-900, 2003.

28 Gettelman, A., Liu, X., Ghan, S. J., Morrison, H., Park, S., Conley, A. J., Klein, S. A., Boyle, J., Mitchell, D. L.,
29 and Li, J. L.: Global simulations of ice nucleation and ice supersaturation with an improved cloud scheme in
30 the Community Atmosphere Model, *J. Geophys. Res. Atmos.*, 115, 2010.

1 Gryspeerdt, E., Sourdeval, O., Quaas, J., Delanoë, J., Krämer, M., and Kühne, P.: Ice crystal number concentration
2 estimates from lidar-radar satellite remote sensing-Part 2: Controls on the ice crystal number concentration,
3 *Atmos. Chem. Phys.*, 18, 14351-14370, 2018.

4 Guignard, A., Stubenrauch, C., Baran, A., and Armante, R.: Bulk microphysical properties of semi transparent
5 cirrus from AIRS: a six years global climatology and statistical analysis in synergy with CALIPSO and
6 CloudSat, *Atmos. Chem. Phys. Discuss.*, 11, doi:10.5194/acpd-11-24671-2011, 2011.

7 He, Q., Zheng, X., Li, J., Gao, W., Wang, Y., Cheng, T., Pu, J., Liu, J., and Li, C.: The role of ASM on the
8 formation and properties of cirrus clouds over the Tibetan Plateau. *Tellus, Ser. B: Chem. Phys. Meteorol.*,
9 71(1), 1577070.

10 Hendricks, J., Kärcher, B., and Lohmann, U.: Effects of ice nuclei on cirrus clouds in a global climate model, *J.*
11 *Geophys. Res. Atmos.*, 116, D18206, 2011.

12 Hoose, C. and Möhler, O.: Heterogeneous ice nucleation on atmospheric aerosols: a review of results from
13 laboratory experiments, *Atmos. Chem. Phys.*, 12, 9817–9854, 2012.

14 Hoose, C., and Möhler, O.: Heterogeneous ice nucleation on atmospheric aerosols: a review of results from
15 laboratory experiments, *Atmos. Chem. Phys.*, 12, 9817-9854, 2012.

16 Huang, J. P., Liu, Y. Z., Wang, T. H., Yan, H. R., Li, J. M., and He, Y. L.: An overview of the aerosol and cloud
17 properties and water vapor budget over the Qinghai-Xizang Plateau, *Plateau Meteor.*, 40, 1225-1240, 2021.

18 Jin, L. J., Yin, Y., Wang, P. X., and Chen, B. J.: Numerical modeling of tropical deep convective anvil and
19 sensitivity test on its response to changes in the cloud condensation nuclei concentration, *Chinese J. Atmos.*
20 *Sci.*, 31, 793-804, 2007.

21 Kärcher, B. and Lohmann, U.: A parameterization of cirrus cloud formation: Heterogeneous freezing, *J. Geophys.*
22 *Res. Atmos.*, 108, doi:10.1029/2002JD003220, 2003.

23 Kay, J. E. and Wood, R.: Timescale analysis of aerosol sensitivity during homogeneous freezing and implications
24 for upper tropospheric water vapor budgets, *Geophys. Res. Lett.*, 35, L10809, 2008.

25 Khain, A., Ovtchinnikov, M., Pinsky, M., Pokrovsky, A., and Krugliak, H.: Notes on the state-of-the-art numerical
26 modeling of cloud microphysics, *Atmos. Res.*, 55, 159-224, 2000.

27 Khvorostyanov, V. I., Morrison, H., Curry, J. A., Baumgardner, D., and Lawson, P.: High supersaturation and
28 modes of ice nucleation in thin tropopause cirrus: Simulation of the 13 July 2002 Cirrus Regional Study of
29 Tropical Anvils and Cirrus Layers case, *J. Geophys. Res. Atmos.*, 111, doi:10.1029/2004JD005235, 2006.

30 Kienast-Sjögren, E., Rolf, C., Seifert, P., Krieger, U. K., Luo, B. P., Krämer, M., and Peter, T.: Climatological and

1 radiative properties of midlatitude cirrus clouds derived by automatic evaluation of lidar measurements,
2 Atmos. Chem. Phys., 16, 7605-7621, 2016.

3 Kim, M. H., Omar, A. H., Tackett, J. L., Vaughan, M. A., Winker, D. M., Trepte, C. R., Hu, Y. X., Liu, Z. Y., Poole,
4 L. R., Pitts, M. C., Kar, J., and Magill, B. E.: The CALIPSO version 4 automated aerosol classification and
5 lidar ratio selection algorithm, Atmo. Meas. Tech., 11, 6107-6135, 2018.

6 Koop, T., and Murray, B.J.: A physically constrained classical description of the homogeneous nucleation of ice in
7 water, J. Chem. Phys., 145, 211915-1-211915-11, 2016.

8 Ladino Moreno, L. A., Stetzer, O., and Lohmann, U.: Contact freezing: a review of experimental studies, Atmos.
9 Chem. Phys., 13, 9745-9769, 2013.

10 Li, Q., Jiang, J. H., Wu, D. L., Read, W. G., Livesey, N. J., Waters, J. W., Zhang, Y., Wang, B., Filipiak, M. J., and
11 Davis, C. P.: Convective outflow of South Asian pollution: A global CTM simulation compared with EOS
12 MLS observations, Geophys. Res. Lett., 32, doi:10.1029/2005GL022765, 2005.

13 Liu, Z., Omar, A., Vaughan, M., Hair, J., Kittaka, C., Hu, Y. X., Powell, K., Trepte, C., Winker, D., Hostetler, C.,
14 Ferrare, R., and Pierce, R.: CALIPSO lidar observations of the optical properties of Saharan dust: A case
15 study of long-range transport, J. Geophys. Res. Atmos., 113, doi: 10.1029/2007JD008878, 2008.

16 Lyu, K., Liu, X., and Kärcher, B.: Exploring sources of ice crystals in cirrus clouds: comparative analysis of two
17 ice nucleation schemes in CAM6, Atmos. Chem. Phys., 25, 15369-15388, 2025.

18 ~~Mamouri, R. E., Ansmann, A., Ohneiser, K., Knopf, D. A., Nisantzi, A., Bühl, J., Engelmann, R., Skupin, A.,~~
19 Seifert, P., Baars, H., Ene, D., Wandinger, U., and Hadjimitsis, D.: Wildfire smoke triggers cirrus formation:
20 lidar observations over the eastern Mediterranean, Atmos. Chem. Phys., 23, 14097-14114, 2023.

21 Mao, F., Shi, R., Rosenfeld, D., Pan, Z., Zang, L., Zhu, Y., and Lu, X.: Retrieving instantaneous extinction of
22 aerosol undetected by the CALIPSO layer detection algorithm, Atmos. Chem. Phys., 22(16), 10589-10602,
23 2022.

24 McCluskey, C. S., DeMott, P. J., Prenni, A. J., Levin, E. J., McMeeking, G. R., Sullivan, A. P., Hill, T. C., Nakao,
25 S., Carrico, C. M., and Kreidenweis, S. M.: Characteristics of atmospheric ice nucleating particles associated
26 with biomass burning in the US: Prescribed burns and wildfires, J. Geophys. Res. Atmos., 119, 10458-10470,
27 2014.

28 Morris, C. E., Georgakopoulos, D. G., and Sands, D. C.: Ice nucleation active bacteria and their potential role in
29 precipitation, J. Phys. IV France., 121,87-103, 2004.

删除[凯]: Maeda, N.: Brief overview of ice nucleation.
Molecules, 26, 392, 2021.

1 Murray, B. J., Broadley, S. L., Wilson, T. W., Bull, S. J., Wills, R. H., Christenson, H. K., Murray, E. J.: Kinetics of
2 the homogeneous freezing of water, *Phys. Chem. Chem. Phys.*, 12, 10380–10387, 2010.

3 Murray, B. J., O'sullivan, D., Atkinson, J. D., and Webb, M. E.: Ice nucleation by particles immersed in
4 supercooled cloud droplets, *Chem. Soc. Rev.*, 41, 6519-6554, 2012.

5 Murray, B. J., Wilson, T. W., Dobbie, S., Cui, Z., Al-Jumur, S. M., Möhler, O., Schnaiter, M., Wagner, R., Benz, S.,
6 and Niemand, M.: Heterogeneous nucleation of ice particles on glassy aerosols under cirrus conditions, *Nat.*
7 *Geosci.*, 3, 233-237, 2010.

8 Prenni, A. J., DeMott, P. J., Sullivan, A. P., Sullivan, R. C., Kreidenweis, S. M., and Rogers, D. C.: Biomass
9 burning as a potential source for atmospheric ice nuclei: Western wildfires and prescribed burns, *Geophys. Res.*
10 *Lett.*, 39, L11805, 2012.

11 Randel, W. J., Park, M., Emmons, L., Kinnison, D., Bernath, P., Walker, K. A., Boone, C., and Pumphrey, H.:
12 Asian monsoon transport of pollution to the stratosphere, *Science*, 328, 611-613, 2010.

13 Shi, X. J., Zhu, S. P., Zhi, X. F., Du, K. Y., Liu, Q. G., and Wang, L. W.: Sensitivity study on three ice nucleation
14 parameterizations, *Trans. Atmos. Sci.*, 40, 181-192, 2017.

15 Shi, X., Liu, X., and Zhang, K.: Effects of pre-existing ice crystals on cirrus clouds and comparison between
16 different ice nucleation parameterizations with the Community Atmosphere Model (CAM5), *Atmos. Chem.*
17 *Phys.*, 15, 1503-1520, 2015.

18 Sourdeval, O., Gryspeerdt, E., Krämer, M., Goren, T., Delanoë, J., Afchine, A., Hemmer, F., and Quaas, J.: Ice
19 crystal number concentration estimates from lidar-radar satellite remote sensing-Part 1: Method and
20 evaluation, *Atmos. Chem. Phys.*, 18, 14327-14350, 2018.

21 Stephens, G. L.: Cloud feedbacks in the climate system: A critical review, *J. Climate.*, 18, 237-273, 2005.

22 Sun, N., Fu, Y., Zhong, L., Zhao, C., & Li, R.: The impact of convective overshooting on the thermal structure over
23 the Tibetan Plateau in summer based on TRMM, COSMIC, Radiosonde, and Reanalysis Data. *J. Climate*, 34,
24 8047-8063, 2021.

25 Wang, C. M., Ye, J. D. and Wei, S. Y.: A numerical experiment of aerosol concentration affecting warm rain
26 process, *Scientia Meteor. Sinica*, 17, 316-323, 1997.

27 Wang, H. Q., and Zhao, G. X.: Cloud and Radiation-I: Cloud climatology and radiative effects of clouds, *Scientia*
28 *Atmos. Sinica*, 18, 910-932, 1994.

删除[凯]: Prabhakara, C., Kratz, D., Yoo, J.-M., Dalu, G.,
and Vernekar, A.: Optically thin cirrus clouds: Radiative
impact on the warm pool, *J. Quant. Spectrosc. Radiat.*
Transfer, 49, 467-483, 1993.

删除[凯]: Takahashi, H. and Luo, Z.: Where is the level of
neutral buoyancy for deep convection? *Geophys. Res. Lett.*, 39,
2012.

1 Wang, K., Chen, J., Hong, Z. C., Yan, C. Q., and He, Q. S.: Research of the distribution characteristics and
2 generation mechanism of cirrus clouds over the Qinghai-Xizang Plateau in summer, *Plateau Meteor.*, doi:10.
3 7522/j. issn. 1000-0534. 2022. 00069, 2023.

4 Xie, S. F., Wang, Y. J., Huang, L. K., Pan, Q. Y., and Wei, P. Z.: Accuracy analysis of Tm calculated by ERA5 and
5 MERRA-2 reanalysis data over China, *J. Geo. Geodyn.*, 41, 771-776, 2021.

6 Xue, X. N., Deng, X. B., and Liu, G. H.: Study on characteristics of Qinghai-Tibetan Plateau cirrus based on
7 satellite data, *Plateau Meteor.*, 37, 505-513, 2018.

8 Yang, Y. K., Zhao, C. F., and Fan, H.: Spatiotemporal distributions of cloud properties over China based on
9 Himawari-8 advanced Himawari imager data, *Atmos. Res.*, 240, doi:10.1016/j.atmosres.2020.104927, 2020.

10 Zhang, F., Yu, Q. R., Mao, J. L., Dan, C., Wang, Y., He, Q., Cheng, T., Chen, C., Liu, D., and Gao, Y.: Possible
11 mechanisms of summer cirrus clouds over the Tibetan Plateau, *Atmos. Chem. Phys.*, 20, 11799-11808, 2020.

12 Zhang, K., Liu, X., Wang, M., Comstock, J. M., Mitchell, D. L., Mishra, S., and Mace, G. G.: Evaluating and
13 constraining ice cloud parameterizations in CAM5 using aircraft measurements from the SPARTICUS
14 campaign, *Atmos. Chem. Phys.*, 13, 4963-4982, 2013.

15 Zhao, B., Liou, K. N., Gu, Y., Jiang, J. H., Li, Q., Fu, R., Huang, L., Liu, X., Shi, X., Su, H., and He, C.: Impact of
16 aerosols on ice crystal size, *Atmos. Chem. Phys.*, 18, 1065-1078, 2018.

17 Zhao, C., Chen, Y., Li, J., Letu, H., Su, Y., Chen, T., and Wu, X.: Fifteen-year statistical analysis of cloud
18 characteristics over China using Terra and Aqua Moderate Resolution Imaging Spectroradiometer
19 observations, *Int. J. Climatol.*, 39, 2612-2629, 2019.

20 Zheng, J. Y., Liu, D., Wang, Z. E., Tian, X. M., Wang, Y. J., and Xie, C. B.: Global distribution and seasonal
21 variation of clouds observed from CloudSat/CALIPSO, *Acta Meteor. Sinica.*, 76, 420-433, 2018.

删除[凯]: Wang, P. H., Minnis, P., McCormick, M. P., Kent,
G. S., and Skeens, K. M.: A 6-year climatology of cloud
occurrence frequency from Stratospheric Aerosol and Gas
Experiment II observations (1985-1990), *J. Geophys. Res.*
Atmos., 101, 29407-29429, 1996.